ACS NANO

www.acsnano.org

Article

Anomalous Heavy Metal Sequestration via MnO_2 Layer-to-Tunnel Transformation

Xinran Liang,* Xinyu Gao, Haoran Hu, Muammar Mansor, Fayang Guo, Bruno Lanson, Lei Wang, Fangdong Zhan, Yanqun Zu, Haesung Jung, Hui Li, Wenfeng Tan, Xionghan Feng,* Biao Wan,* and James J. De Yoreo

Cite This: *ACS Nano* 2026, 20, 11344–11357

Read Online

ACCESS | Metrics & More | Article Recommendations | Supporting Information

ABSTRACT: Crystallization of poorly crystalline minerals generally remobilizes the adsorbed heavy metals. In contrast, we find that the conversion of poorly crystalline layered δ-MnO_2 to crystalline 2 × 2 tunneled α-MnO_2 significantly increases both the amount and stability of Pb^{2+} immobilization. The varied characterization analyses reveal that Pb^{2+} first exchanges surface K^+ associated with δ-MnO_2 and is then sequestered into α-MnO_2 2 × 2 tunnels via oriented attachment along the (001) plane. Without the crystallization process, Pb^{2+} cannot substitute for tunnel K^+ in α-MnO_2 and can only weakly bind to the external (310) surface. Stability comparisons across outer-surface adsorption, wall substitution, and tunnel incorporation indicate that only tunnel-resident metals achieve strongly enhanced and persistent Pb sequestration. This study not only challenges the conventional understanding that mineral crystallization and layer-to-tunnel transformation lead to the release of adsorbed heavy metals but also suggests a potential strategy for selective metal trapping in engineered remediation materials and environmental matrices.

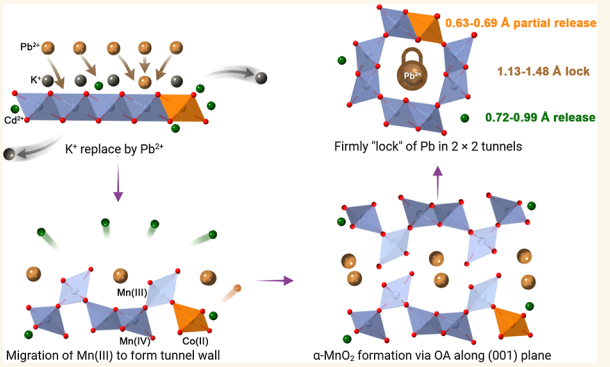

KEYWORDS: *manganese oxides, heavy metal, sequestration, crystallization, oriented attachment*

INTRODUCTION

Heavy metal contamination, particularly within agricultural systems, poses a persistent and serious risk to human health and environmental sustainability.[1] Although substantial progress has been made in understanding the adsorption mechanisms of heavy metals by soil minerals/materials,[2−4] the adsorption of metal ions onto adsorbent surfaces does not represent the end point of their biogeochemical cycling on earth's surface. The dynamic and fluctuating properties of environmental conditions can induce the coupled structural and morphological transformations of adsorbent matrices or materials.[3,5] These alterations can profoundly influence the environmental fate of the bound metals via modifying their mobility, bioavailability, and potential toxicity.[2−4]

Poorly crystalline adsorbents, such as iron (Fe) oxides, manganese (Mn) oxides, and layered double hydroxides (LDHs), are usually applied to capture large amounts of heavy metals in wastewater treatment and soil decontamination systems due to their high specific surface area (SSA), abundant adsorption sites, and excellent sequestration ability.[5−7] After the crystallization, these minerals undergo an atomic rearrangement into the crystalline counterparts that significantly decrease their SSA and available adsorption sites. This structural transformation often triggers the secondary release of previously immobilized heavy metals.[8,9] For example, the poorly crystalline Fe and Mn oxides have been found to adsorb more Pb^{2+} and Cd^{2+} than their well-crystallized counterparts, primarily due to their larger SSA.[10] Similarly, biogenic α-Mn_2O_3 with low crystallinity adsorbs greater amounts of Pb^{2+}, Cd^{2+}, Cu^{2+}, Zn^{2+}, and Ni^{2+} compared to synthetic α-Mn_2O_3 with higher crystallinity and lower SSA.[11] The transformation of poorly crystalline Fe_3O_4 into highly crystalline α-Fe_2O_3 or γ-Fe_2O_3 significantly reduces its capacity to immobilize Cd^{2+} and Pb^{2+}.[12]

In addition to crystallization, the phase transformation from a 2-D layered structure to a 1-D tunnel structure typically results in less accessible interlayer or internal surface sites, and thus lower adsorption capacity. For example, about half of the Ni^{2+} preretained in Na-buserite was released when it transformed into todorokite (a 1-D tunnel-structured Mn oxide with a 3 × 3 tunnel arrangement).[13] A similar release of Co^{3+} was observed when cobalt-doped layered buserite

Received: January 16, 2026
Revised: March 28, 2026
Accepted: March 30, 2026
Published: April 3, 2026

https://doi.org/10.1021/acsnano.6c00961
ACS Nano 2026, 20, 11344−11357

Table 1. Summary of the Experimental Conditions and the 30 day Solid Products, and Their Labels[a]

treatment	initial structure	[Mn(II)]/[MnO_2]	heavy metal	dissolved M(X) (mM)	sample label
the experimental conditions	δ-MnO_2	0	Pb	3	Pb_δ-MnO_2_Adsorption
	δ-MnO_2	~0.36	Pb	3	Pb_δ-MnO_2_Aging
	α-MnO_2	0	Pb	3	Pb_α-MnO_2_Adsorption
	δ-MnO_2	~0.36	Cd	3	Cd_δ-MnO_2_Aging
	δ-MnO_2	~0.36	Co	3	Co_δ-MnO_2_Aging
the solid products after a 30 day reaction	δ-MnO_2	0	Pb	3	Pb_δ-MnO_2_ads
	δ-MnO_2	~0.36	Pb	3	Pb_α-MnO_2_tun#
	α-MnO_2	0	Pb	3	Pb_α-MnO_2_ads
	δ-MnO_2	~0.36	Cd	3	Cd_α-MnO_2_ads#
	δ-MnO_2	~0.36	Co	3	Co_α-MnO_2_sub#
the solid products after a 7 day reaction	δ-MnO_2	~0.36	Zn	3	Zn_α-MnO_2_ads#
	δ-MnO_2	~0.36	Ba	3	Ba_α-MnO_2_tun#
	δ-MnO_2	~0.36	Ag	3	Ag_α-MnO_2_tun#

[a]"ads" = metal adsorbed on the mineral surface; "tun" = metal encapsulated in the 2 × 2 tunnels of α-MnO_2; "sub" = metal substituting Mn in the [MnO_6] framework at the tunnel walls of α-MnO_2. The "#" symbol denotes α-MnO_2 produced by Mn^{2+}-induced transformation of δ-MnO_2 preloaded with heavy metal ions (e.g., Pb^{2+}/Cd^{2+}/Co^{2+}) into α-MnO_2.

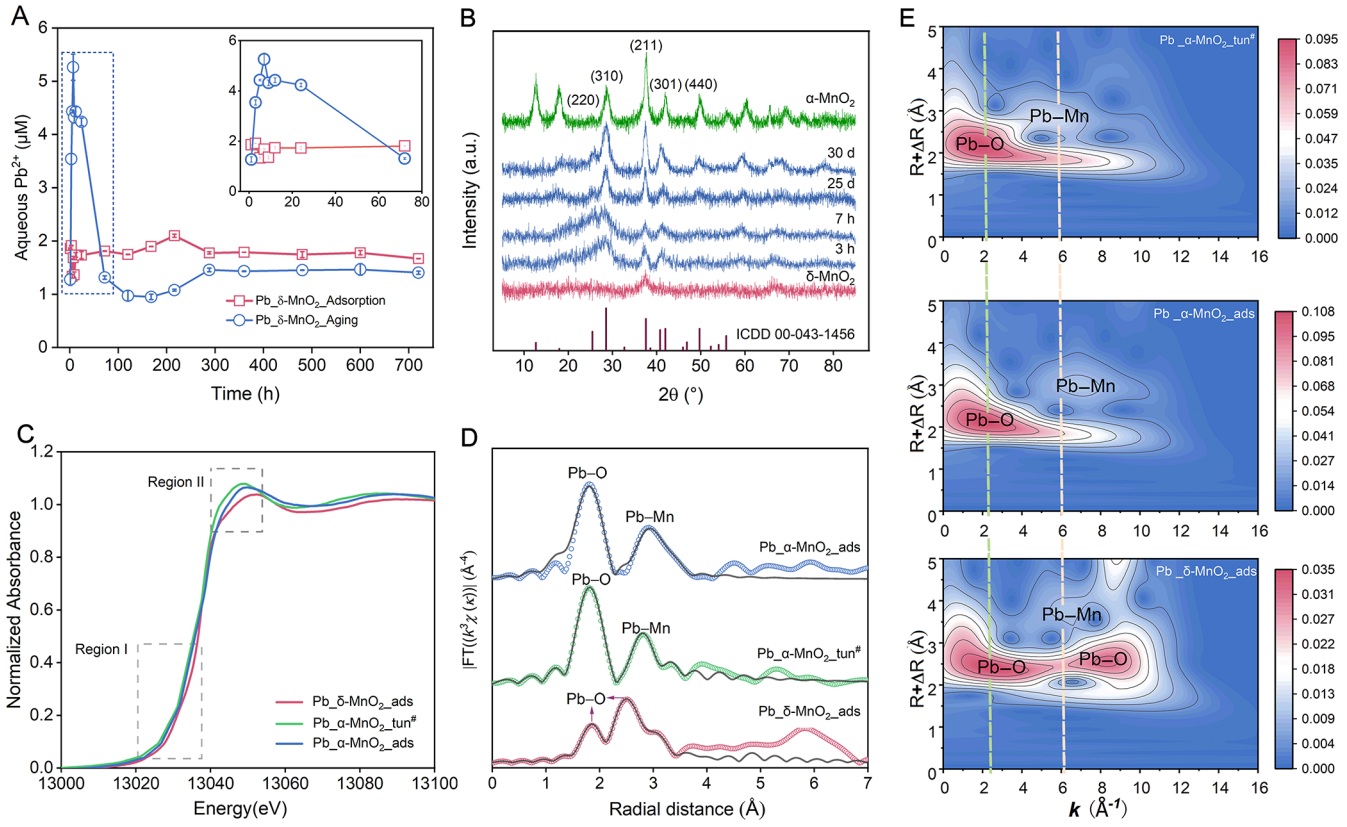

Figure 1. Pb^{2+} adsorption on layered δ-MnO_2 and tunneled α-MnO_2 formation during Mn^{2+}-induced aging at pH 4. (A) Dynamics of aqueous Pb^{2+} concentration change during Pb^{2+} adsorption on δ-MnO_2 and Mn^{2+}-induced δ-MnO_2 aging in the presence of Pb^{2+} at pH 4. (B) Time-resolved XRD patterns of solid products from Mn^{2+}-induced δ-MnO_2 aging samples in the presence of Pb^{2+} at pH 4. Coronadite (ICDD no. 00-043-1456), raw δ-MnO_2, and synthetic α-MnO_2 are included as references. (C) Pb L_3-edge XANES of Pb_δ/α-MnO_2_ads and Pb_α-MnO_2_tun# samples at pH 4 (Table 1). (D) Fourier transform of k^3-weighted Pb L_3-edge EXAFS and its fitting results in *R* space. The gray line and colorful cycles represent the fitting results and initial data, respectively. (E) Wavelet transform of k^3-weighted Pb L_3-edge EXAFS. The concentrations of δ-MnO_2 (2.4 g/L) and Pb^{2+} (3 mM), and the molar ratio of [Mn^{2+}]/[δ-MnO_2] (~0.36) are used.

transformed into todorokite.[14] Therefore, the transformation either from layer to tunnel phases or from poorly crystalline adsorbents with high SSA to highly crystalline phases with low SSA often results in the massive release of previously surface-fixed heavy metals.

δ-MnO_2, the most common natural Mn oxide with a 2-D layered structure and weak crystallinity, shows a strong affinity for Pb^{2+} in natural environments.[15] It shows strong Pb^{2+} adsorption primarily occurring at vacancies on the (001) basal plane and edge sites on the (100) plane.[15] However, the sequestration of Pb^{2+} by δ-MnO_2 is not always permanent. In nature, δ-MnO_2 often acts as a precursor to other Mn oxides through structural transformations driven primarily by Mn^{2+}-induced reductive-disproportionation reactions. For example,

https://doi.org/10.1021/acsnano.6c00961
ACS Nano 2026, 20, 11344−11357

at pH 4, Mn^{2+} adsorbed into structural vacancies easily triggers the conversion of δ-MnO_2 into cryptomelane, a tunnel-structured α-MnO_2 with a 2 × 2 framework and pore size of 4.6 Å.[16,17] Under neutral pH conditions, δ-MnO_2 is reductively transformed into manganite (γ-MnOOH) in the presence of Mn^{2+}.[18] At higher pH values above 8.5, it further transforms into hausmannite (Mn_3O_4).[18] When compared to δ-MnO_2 (1832 mmol/kg), these secondary Mn oxides exhibit remarkably lower Pb^{2+} adsorption capacities (α-MnO_2 at 292.8 mmol/kg, γ-MnOOH at 284.3 mmol/kg, and Mn_3O_4 at 105.3 mmol/kg).[15,19] This wide-range variation highlights an important environmental concerns during heavy metal remediation by Mn-bearing materials: as δ-MnO_2 easily transforms into other Mn oxides, its ability and reactivity to retain Pb^{2+} decreases, likely increasing the remobilization risk of the stabilized Pb^{2+}.

It remains uncertain whether typical heavy metals are released or not during the Mn oxide crystallization, representing a key knowledge gap in understanding the behavior of heavy metals in dynamic mineral transformations. In this study, to elucidate the potential mechanism of secondary Pb^{2+} release following its adsorption by δ-MnO_2, δ-MnO_2 was first synthesized and washed, followed by Mn^{2+} induction of structural transformation. A comprehensive suite of advanced analytical techniques was employed to characterize the structural transitions and morphological evolutions of δ-MnO_2. These analytic techniques include X-ray diffraction (XRD), X-ray absorption fine structure spectroscopy (XAFS), high-resolution transmission electron microscopy (HRTEM), field-emission scanning electron microscopy (FESEM), and aberration-corrected scanning HRTEM (A-HRTEM). In addition, density functional theory (DFT) simulations were employed to complement experimental observations and calculate Pb binding energies. This multidisciplinary approach provides a mechanistic understanding of Pb^{2+} sequestration and release controlled by Mn oxide mineralogical transformation. These insights advance our current mechanistic knowledge about Pb^{2+} geochemical cycling at soil mineral interfaces and carry significant implications for predicting heavy metal mobility or sequestration in Mn-rich environmental matrices or Mn-based remediation fields.

RESULTS AND DISCUSSION

Anomalous Pb^{2+} Sequestration during δ-MnO_2 Transformation to α-MnO_2

To justify the effect of mineral structural transformation on heavy metal sequestration, we monitored the change of aqueous Pb^{2+} concentrations over a 30 day reaction under two typical treatments: (i) 3 mM Pb^{2+} adsorption onto synthetic δ-MnO_2 and (ii) Mn^{2+}-induced aging of layered δ-MnO_2 with adsorbed Pb^{2+} at pH 4 (Table 1 and Figure 1A). Over 30 day adsorption on δ-MnO_2, the aqueous Pb^{2+} was maintained at a low concentration around 1−2 μM, implying the high metal sequestration capacity of δ-MnO_2. When Mn^{2+} was introduced, the adsorbed Pb^{2+} was slightly released in the first 7 h, with the concentration increasing from 1 to 5 μM (about 3 mM Pb^{2+} was added). The initial increase in the concentration of dissolved Pb^{2+} may derive from the competitive adsorption of the introduced Mn^{2+} with the preadsorbed Pb^{2+} on δ-MnO_2 surface sites.[20] The dissolved Pb^{2+} concentration then decreased after 9 h. After 3 days, the Pb^{2+} concentration during Mn^{2+}-induced δ-MnO_2 transformation stayed at a lower level than that of Pb^{2+} adsorption on δ-MnO_2. During the 3 to 30 day reaction (e.g., crystallization), the Pb^{2+} concentration in both treatments was always below 2 μM (Figure 1A). Meanwhile, SEM−EDS images showed the copresence of Mn and Pb signals in both Pb_δ-MnO_2_ads and Pb_α-MnO_2_tun sample particles (Figure S1). These results suggested that the newly formed Mn oxides still maintain anomalous Pb sequestration even after δ-MnO_2 transformation.

At the same time, the dissolution of δ-MnO_2 during the Pb^{2+} adsorption and the immobilization of Mn^{2+} on δ-MnO_2 (Figure S2) were measured over the 30 day reaction. After an hour of the Mn^{2+} addition into the suspension of Pb^{2+} adsorbed δ-MnO_2, aqueous Mn^{2+} concentration rapidly decreased from 10 mM to 0.54 mM. The concentration of Pb^{2+} merely increased from 1 μM to 5 μM, which was remarkably less than the Mn^{2+} adsorption amount. During the Pb^{2+} adsorption in the absence of Mn^{2+}, no obvious Mn^{2+} dissolution was detected. This further supports the competitive adsorption effect induced by Mn^{2+} mentioned above. However, compared to the amounts of Pb^{2+} release and Mn^{2+} added, the competitive adsorption effect is very limited. The Mn^{2+} competitive adsorption cannot completely explain the change of Pb^{2+} concentration, particularly with the reimmobilization of Pb^{2+} after 24 h (Figure 1A). Previous studies indicated that the presence of Mn^{2+} induced the transformation of layered δ-MnO_2 to the tunneled α-MnO_2,[17,21] being potentially suitable to explain Pb resequestration. Therefore, the structural and morphological analyses of the newly formed Mn oxides were performed to elucidate the reasons behind the anomalous Pb^{2+} sequestration and the Pb^{2+} associated coordination sites, which will provide the mechanistic understanding of Pb^{2+} stabilized immobilization by the various Mn remediation materials.

Structural and Morphological Analyses of Pb^{2+} Association on the Newly Formed Mn Oxides

Time-resolved XRD patterns of Mn^{2+}-induced δ-MnO_2 (with preadsorbed Pb^{2+}) transformation products were measured to identify the structural transformation phases over a 30 day reaction at pH 4. Figure 1B displays that a diffraction peak corresponding to Pb_α-MnO_2_tun sample and synthetic α-MnO_2 appears at 28.5° ($d_{(301)}$ = 0.31 nm) after 3 h, implying the rapid and possible transformation of δ-MnO_2 into α-MnO_2 induced by Mn^{2+} (Figure S2).[17] As the reaction progressed, the characteristic diffraction of Pb_α-MnO_2_tun was observed at 25.5° ($d_{(-202)}$ = 0.35 nm), 28.5° ($d_{(301)}$ = 0.31 nm), and 40.8° ($d_{(402)}$ = 0.22 nm), suggesting that the newly formed Mn oxide is α-MnO_2. The intensities and sharpness of these diffractions greatly enhanced on the 30th day, indicating increased crystallinity and particle growth of the newly formed Mn oxides. In comparison to the formed tunnel-structured α-MnO_2 (reported SSA = 21.3 m^2/g), δ-MnO_2 has lower crystallinity with an open 2-D interlayer space and a large specific surface area (reported SSA = 81.45 ± 2.63 m^2/g), potentially possessing a high Pb^{2+} adsorption capacity.[19,22] As shown in Figure 1A, the Pb^{2+} sequestration in the Mn^{2+}-induced δ-MnO_2 transformation suspension was close to the system in which no mineral transformation occurred. One possible explanation is that Pb^{2+} may have entered the tunnel structure of the newly formed α-MnO_2 phase, since synthetic α-MnO_2 only adsorbed a very small amount of Pb^{2+} (Table S1).

https://doi.org/10.1021/acsnano.6c00961
ACS Nano 2026, 20, 11344−11357

Table 2. Shell-by-Shell EXAFS Fitting Parameters of 30 day Reaction Solid Samples and the Standard References

samples	path	CN[a]	R (Å)[b]	σ^2 (Å^2)[c]	ΔE_0 (eV)[d]	R factor
		Pb L_3-edge (S_0^2 = 0.877)				
Pb foil	Pb−Pb	6.0[e]	3.361	0.0190	−8.4	0.0192
	Pb−Pb	6.0[e]	3.935	0.0278	−2.9	
$PbSO_4$	Pb−O	5.3	2.646	0.0040	−7.1	0.0155
	Pb−O	3.3	2.841			
	Pb−S	7.9	4.103	0.0217	0.1	
Pb_α-MnO_2_ads	Pb−O	4.6	2.337	0.0098	−4.5	0.0181
	Pb−Mn	2.2	3.431	0.0082	−12.4	
Pb_δ-MnO_2_ads	Pb−O	2.2	2.365	0.0042	−2.5	0.0020
	Pb−O	3.8	2.857			
	Pb−Mn	3.0	3.452	0.0119	−4.1	
Pb_α-MnO_2_tun	Pb−O	3.7	2.329	0.0079	−3.4	0.0178
	Pb−Mn	5.3	3.396	0.0234	−6.4	

[a]CN, coordination number. [b]R (Å), the distance between absorber and backscatter atoms (phase corrected for first shell scatterers). [c]σ^2, the Debye−Waller factor value. [d]ΔE_0, inner potential correction to account for the difference in the inner potential between the sample and the reference compound; R factor indicates the goodness of the fit. S_0^2 was fixed at 0.877, according to the experimental EXAFS fit of Pb foil by fixing CN as the known crystallographic value. [e]This value was fixed during EXAFS fitting, based on the known structure of Pb. Fitting conditions: k range: 3.0−10.0; R range: 1.8−4.0; fitting space: R space; k-weight = 3. A reasonable range of EXAFS fitting parameters: 0.800 < S_0^2 < 1.000; CN > 0; σ^2 > 0 Å^2; $|\Delta E_0|$ < 15 eV; R factor < 0.02.

To identify Pb binding sites and coordination environments, Pb L_3-edge EXAFS spectroscopy was applied to measure the Pb_α-MnO_2_tun sample in comparison with the Pb_α-MnO_2_ads and Pb_δ-MnO_2_ads samples, which were used to confirm further whether Pb was located within the α-MnO_2 tunnel structure or not (Figures 1C,D and S3). Pb L_3-edge XANES spectra showed that Pb_δ-MnO_2_ads had the weakest Pb L_3-edge white-line intensity due to its distorted low-coordination environment, while Pb_α-MnO_2_tun exhibited the strongest white-line signal, likely resulting from its highly symmetrical and fully coordinated structure of Pb incorporation within α-MnO_2 tunnels (Figure 1C). While white-line intensity is sensitive to a complex interplay of factors, including the density of unoccupied states, coordination symmetry, and multiple-scattering contributions, the observed intensity enhancement of Pb_α-MnO_2_tun may be attributed to a more symmetrical and highly coordinated environment, as would be expected for Pb^{2+} stabilization within α-MnO_2 tunnels.[23] Nevertheless, given the inherent complexity of interpreting white-line variations, this observation is treated as a preliminary indication of tunnel incorporation, which will be further corroborated by the following HAADF-STEM and acid-dissolution results to provide direct structural evidence. The Pb L_3-edge EXAFS spectrum of the Pb_δ-MnO_2_ads revealed two distinct Pb−O coordination shells with fitted bond distances of 2.365 Å (R + ΔR) and 2.857 Å (R + ΔR) (corresponding to raw distances at 1.84 Å and 2.51 Å within a radial distance of 4 Å in Figure 1D), along with coordination numbers of 2.2 and 3.8 (Table 2), respectively. An additional Pb−Mn shell associated with Pb complexation on δ-MnO_2 features a fitted Pb−Mn distance of 3.452 Å (R + ΔR) (corresponding to a raw distance at 3.12 Å) with an estimated coordination number of approximately 3.0. As a comparison, both the Pb_α-MnO_2_tun and Pb_α-MnO_2_ads exhibit a single Pb−O coordination shell with fitted Pb−O distances of 2.329 Å (R + ΔR) and 2.337 Å (R + ΔR) (corresponding to raw distances at 1.81 Å and 1.82 Å), and coordination numbers of 3.7 and 4.6, respectively. The Pb L_3-edge EXAFS spectrum of Pb_α-MnO_2_tun shows that the fitted Pb−Mn bond distance is 3.396 Å (R + ΔR) with a bigger coordination number of 5.3, indicative of Pb resequestration in the tunnels. The Pb L_3-edge EXAFS spectrum of Pb_α-MnO_2_ads shows that the fitted Pb−Mn distance is 3.431 Å (R + ΔR) with a smaller coordination number of 2.2 (Table 2).

Wavelet transformed (WT) EXAFS spectroscopy enables distinguishing the heavier and lighter backscattering atoms with high resolution in both k and R space efficiently. WT EXAFS analysis of Pb_α-MnO_2_tun shows the intensity maximum of Pb−Mn at $k \approx 5.9$ Å^{-1}, which is distinct from the feature of Pb_α-MnO_2_ads ($k \approx 7.2$ Å^{-1}) (Figure 1E). The Pb_α-MnO_2_tun shows the intensity of the maximum of Pb−O at $k \approx 2.2$ Å^{-1}, which is lower than the feature of Pb_α-MnO_2_ads ($k \approx 2.4$ Å^{-1}), Pb_δ-MnO_2_ads ($k \approx 3.1$ Å^{-1}), and $PbSO_4$ ($k \approx 4.9$ Å^{-1}, possible impurities) (Figures 1E and S4). The maximum associated with both the Pb−O and Pb−Mn shells shifts toward lower k after mineral aging, indicating a stronger damping of the high-k EXAFS contributions. This trend is difficult to reconcile with a scenario where Pb^{2+} remains merely adsorbed on the external surfaces of δ-MnO_2 or α-MnO_2, because surface complexation typically preserves relatively well-defined coordination geometries and does not show a systematic loss of high-k intensity for both shells.[14] Instead, the concurrent k-shift of the Pb−O and Pb−Mn WT features is more consistent with Pb^{2+} being structurally incorporated into the 2 × 2 tunnels of α-MnO_2. Within these tunnels, Pb^{2+} occupies off-center positions in a defect-rich charge-compensated environment, which generates a broad distribution of Pb−O and Pb−Mn distances and remarkably increases the Debye−Waller factors. This enhanced static disorder efficiently suppresses the high-k EXAFS components for both coordination shells, thereby justifying that Pb is predominantly hosted within α-MnO_2 tunnels rather than adsorbed on δ-MnO_2 or α-MnO_2 surfaces.[24] These observations were consistent with the XRD result of new coronadite (Pb_α-MnO_2_tun) phase formation, providing solid evidence to support that Pb^{2+} is not only adsorbed on the surface but also mainly incorporated into the tunnel structure of α-MnO_2, finally achieving the greater Pb retention and structural stabilization.

https://doi.org/10.1021/acsnano.6c00961
ACS Nano 2026, 20, 11344−11357

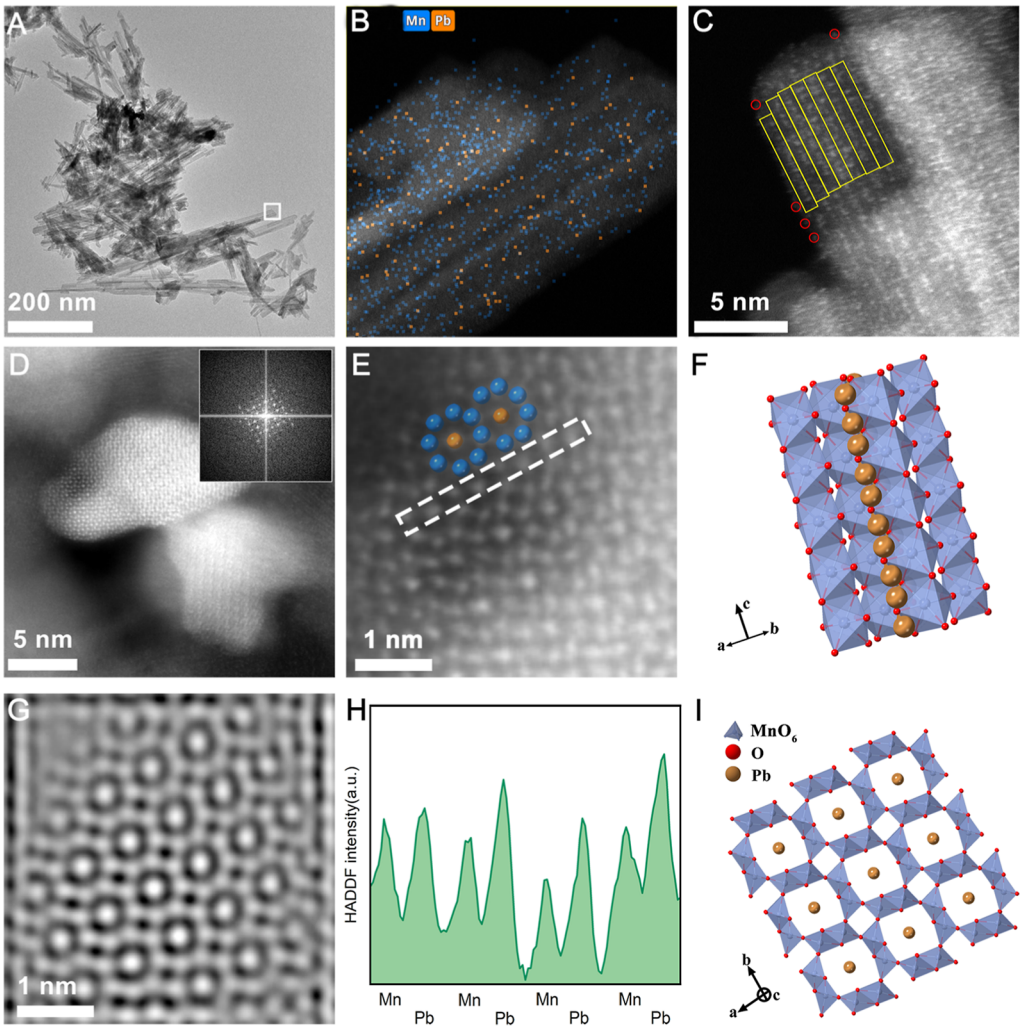

Figure 2. Structural and elemental characterization of the 30 day reaction solid product Pb_α-MnO_2_tun#. (A) The HRTEM image of the 30 day solid product Pb_α-MnO_2_tun#; (B) elemental distribution mapping of the selected region (the white square in Figure 2A); (C) aberration-corrected STEM image of this sample's external surface. The red circles indicate Pb^{2+} adsorption on the outer surface of the MnO_2 nanorods, while the yellow rectangles indicate Pb embedding into the α-MnO_2 tunnel structure aligned in a straight row. (D) The STEM image of the solid product (001) plane of Pb_α-MnO_2_tun# sample at pH 4. The FFT image is inserted. (E) Magnified atomic-resolution STEM and (F) molecular schematic corresponding to the yellow rectangles, showing Pb embedding alignment at the atomic level in Figure 2C. (G) IFFT images of Figure 2E and (H) line profile of the AC-STEM image corresponding to the white rectangle in Figure 2E. (I) Molecular schematic illustration of this sample for Pb sequestration in the tunnel structure of the newly formed α-MnO_2 minerals. The blue octahedra represent [MnO_6] octahedra. Yellow balls represent the tunneled Pb atoms.

To further confirm the presence of Pb^{2+} within the tunnels of the newly formed α-MnO_2, AC-HRTEM imaging and morphological analyses were performed on the (001) plane of Pb_α-MnO_2_tun sample. Due to the short length (approximately 100−300 nm) of the α-MnO_2 nanorods (Figures 2A and S5), it was difficult to prepare a suitable ultramicrotomy or focused ion beam (FIB) sample for microscopic measurement. Instead, a prolonged search was carried out by AC-HRTEM (Figure 2A−G), and a Pb_α-MnO_2_tun sample with the (001) crystal plane oriented perpendicular to the electron beam was successfully identified. This enabled direct visual confirmation that Pb had entered the tunnels of the α-MnO_2 structure (Figure 2B−G). Figure 2E−G show that Pb_α-MnO_2_tun nanorods contain well-defined 0.69 × 0.69 nm tunnels. STEM *Z*-contrast image displays the brighter sites on particle surfaces (Figure 2C, red circles) and at tunnel centers (Figure 2C, yellow rectangles). HAADF images are often described as *Z*-contrast (atomic number) imaging since the measured intensity is approximately proportional to the square of the atomic number. Therefore, these brighter spots can be assigned to Pb atoms binding to the newly formed α-MnO_2.

Profiling the Mn−Pb chain in Figure 2E (white rectangle) reveals the higher HAADF intensity of some Pb spots, which is attributed to the higher atomic number of Pb in the tunnel structure of the nanorod (Figure 2H). The atomic arrangement forms a 2 × 2 tunnel ring around each bright site (Figure 2E). The IFFT image (Figure 2G) aligns with the crystallographic model of Pb_α-MnO_2_tun (Figure 2E), confirming the coordination of each encapsulated Pb atom by eight Mn atoms. STEM−EDS mapping across the (001) plane reveals a strong Pb signal, whereas K remains near the detection limitation (Figures 2B, S6, and S7). These results directly confirm that Pb atoms occupy the tunnel sites. In contrast to the synthetic K-bearing α-MnO_2 in previous studies, the K atom signal at the tunnel center of α-MnO_2 is substantially weaker than the Pb atom signal.[25−27] The detailed analysis of

https://doi.org/10.1021/acsnano.6c00961
ACS Nano 2026, 20, 11344−11357

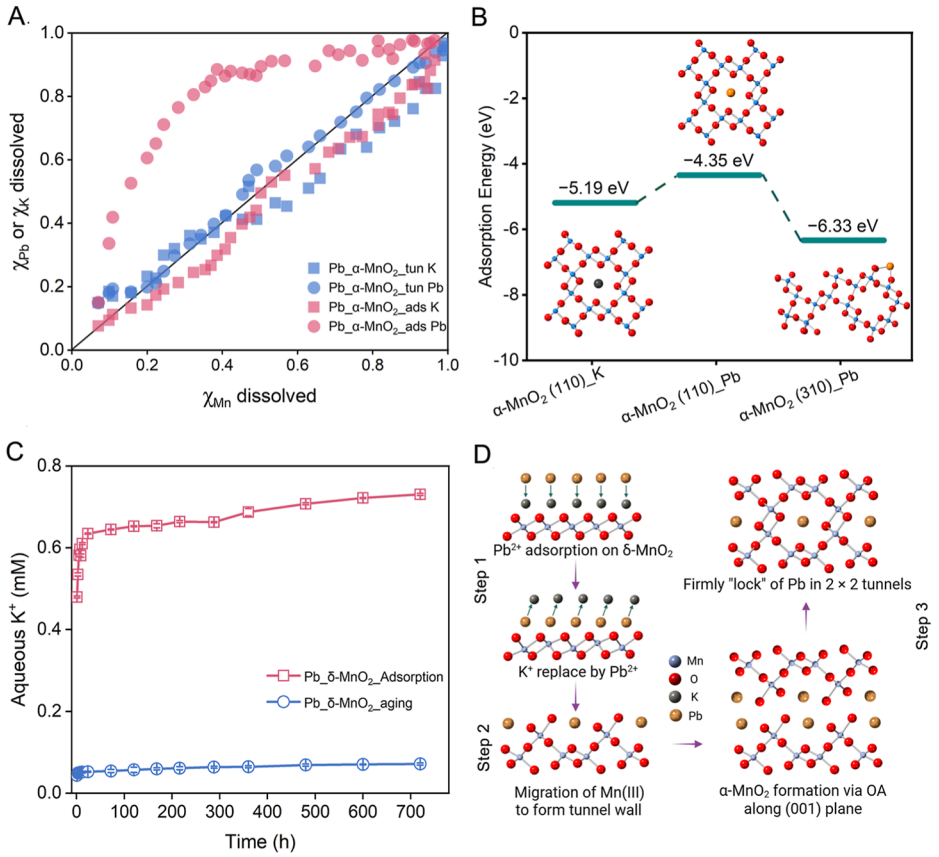

Figure 3. Pb^{2+} sequestration in the α-MnO_2 tunnel during Mn^{2+}-induced transformation, where Pb^{2+} replaces K^+ in δ-MnO_2. (A) Dissolution proportion of Pb, K, and Mn using 2 M HCl to completely dissolve the Pb_α-MnO_2_ads and Pb_α-MnO_2_tun[#] samples. (B) DFT calculations were applied to obtain the binding energies of Pb adsorption on the α-MnO_2(310) surface and those of K^+ and Pb^{2+} incorporation into the (110) tunnel of synthetic and newly formed α-MnO_2. (C) Dynamics of aqueous K^+ concentration change during Pb adsorption on δ-MnO_2 and Mn^{2+}-induced δ-MnO_2 aging in the presence of Pb^{2+} at pH 4. (D) A schematic illustration of Pb^{2+} was "stably locked" during Mn^{2+}-induced aging and transformation of δ-MnO_2 (the layered structure) into α-MnO_2 (the tunneled structure).

Figure 2E,G further reveals that the ~0.69 nm Pb−Pb spacing well matches the (110) lattice plane of α-MnO_2. Within the yellow rectangle in Figure 2C, multiple Pb atoms are seen aligning along the tunnel axis, forming the ordered nanorod-like tunnel arrangement (Figure 2F). This indicates that tunnel encapsulation is the predominant mechanism for Pb^{2+} resequestration and stabilization on the newly formed α-MnO_2 (Figure 2F,I). In addition, a small portion of Pb^{2+} is located at external sites, as indicated by the red circles in HAADF-STEM mapping (Figure 2C), consistent with the previous report of the relatively low Pb^{2+} adsorption capacity of α-MnO_2 external surface sites.[19] In summary, the XRD, Pb L_3-edge EXAFS, and AC-HRTEM results demonstrate that the predominant fraction of Pb^{2+} ions is structurally confined within the 2 × 2 tunnel framework of the newly formed α-MnO_2 from δ-MnO_2 recrystallization induced by Mn^{2+}.

The Stabilization Difference of Pb^{2+} Resequestration on the Surface vs within the Tunnel Structure of α-MnO_2

A substantial amount of Pb^{2+} ions can be stably immobilized through the incorporation into the tunnel structure of α-MnO_2. However, the stabilization difference of tunnel-incorporated Pb^{2+} vs surface-adsorbed one is expected to significantly influence the mobility and long-term fate of Pb^{2+} in the environment. To clarify the difference, acidic dissolution experiments were performed to directly compare the release behaviors of Pb^{2+} from tunnel sites and surface adsorption sites (Figure 3A). The complete dissolution of both Pb_α-MnO_2_ads and Pb_α-MnO_2_tun was observed using 2 M HCl. After complete dissolution of 0.2 g Pb_α-MnO_2_tun and Pb_α-MnO_2_ads, the aqueous Mn^{2+} concentrations were measured to be 3.30 mM and 3.21 mM, suggesting similar dissolution behavior of Mn^{2+} from both samples (Table S1). Crucially, the final Pb^{2+} concentration released from Pb_α-MnO_2_tun was nearly an order of magnitude higher than that from Pb_α-MnO_2_ads (0.36 mM vs 0.03 mM) (Table S1). The calculated sequestration capacity of the transformation-derived Pb_α-MnO_2_tun is 260.0 mg/g, which is approximately 12 times higher than the adsorption capacity of the synthesized Pb_α-MnO_2_ads (22.3 mg/g). This significant discrepancy in Pb sequestration extends, coupled with a ten times lower K^+ release in the Pb_α-MnO_2_tun sample (0.02 mM vs 0.27 mM) (Table S1), directly suggests a cation-exchange mechanism. This result implies that the Pb^{2+} in Pb_α-MnO_2_tun is not only adsorbed but also bound at additional sites beyond simple surface complexation.

The trend of the dissolution curve was also interpreted to reflect the position and stabilization of Pb^{2+} sequestration (Figure 3A). At selected time intervals during Pb_α-MnO_2_tun and Pb_α-MnO_2_ads acidic dissolution, the release of Pb^{2+} adsorbed on the surface of α-MnO_2 is more prone than that of Pb^{2+} incorporated within the tunnels of α-MnO_2. During the Pb_α-MnO_2_ads dissolution, convex $\chi_{Pb/K}/\chi_{Mn}$ curves indicate the accumulation of these Pb and K ions

https://doi.org/10.1021/acsnano.6c00961
ACS Nano 2026, 20, 11344−11357

on the surface of α-MnO_2 minerals and the easy release of Pb^{2+} upon α-MnO_2 dissolution. During the Pb_α-MnO_2_tun dissolution, the straight line of $\chi_{Pb/K}/\chi_{Mn}$ with a slope of 1 suggests that the Pb and K ions are mainly and uniformly incorporated within the tunnel structure of α-MnO_2,[28] since only the structural destruction of the α-MnO_2 crystal can release these ions. This result indicates that Pb^{2+} incorporated within the α-MnO_2 tunnels is more stable than surface-adsorbed Pb^{2+}. Its stability is closer to that of isomorphic substitution in reported studies,[14,28] and agrees well with the Pb coordination structure revealed by Pb L_3-edge EXAFS analysis (Figure 1D).

In addition, DFT calculations were applied to elucidate the differences in Pb^{2+} stability by comparing the binding energies at distinct coordination sites of Pb and K (Figure 3B). The binding energy of K^+ and Pb^{2+} into the 2 × 2 tunnel of α-MnO_2 was calculated to be −5.19 eV and −4.35 eV, respectively. The adsorption energy of Pb^{2+} on the external (310) surface of α-MnO_2 was −6.33 eV, indicating a more favorable thermodynamic driving force for surface complexation than tunnel incorporation. This also suggests that Pb^{2+} adsorbed on the surface of α-MnO_2 binds more strongly than Pb^{2+} incorporated within the tunnels, in agreement with a previous report that the (310) surface of α-MnO_2 exhibits superior selective adsorption of Pb^{2+}.[29] However, this is inconsistent with acidic dissolution experiments, which show that surface-bound Pb^{2+} is released more readily than within the tunnels. A possible explanation for this difference is that the tunnel structure imposes a structural constraint on the ions located within the one-dimensional tunnels, restricting their diffusion and release until the surrounding Mn and O framework is destroyed. This interpretation is supported by acidic dissolution experiments, where substituting the tunnel ions with K^+ resulted in a release curve similar to that of Pb^{2+} (Figure 3A). The metal ions sequestered within the 2 × 2 tunnel structure of α-MnO_2 represent a more effective immobilization mechanism than surface adsorption.

The Mechanism of Pb^{2+} Entry into the Tunnels of α-MnO_2

Since metal incorporation into the tunnel structure is a more effective way to immobilize metal ions, understanding how these ions enter the tunnels becomes a key question. Previous studies have shown that Pb^{2+} adsorption on α-MnO_2 results in only a small amount of Pb^{2+} being retained on the surface and no mineral phase transformation.[19,29] Here, we did not observe the phase change of Mn oxides during Pb^{2+} adsorption on α-MnO_2 and δ-MnO_2 over a 30 day reaction (Figures S7). DFT calculations indicate that the binding energy of K^+ within the (110) tunnel surface is −5.19 eV, which is lower than that of Pb^{2+} (−4.35 eV) (Figure 3B). Therefore, the substitution of K^+ by Pb^{2+} within the tunnels of K-bearing α-MnO_2 to form Pb_α-MnO_2_tun is thermodynamically unfavorable. After 30 days of Pb^{2+} adsorption by synthetic K-bearing α-MnO_2 at pH 4, XRD patterns showed that the structure of α-MnO_2 did not transform into any other Mn oxide phases (Figure S7A). Dissolution of Pb_α-MnO_2_ads product reveals that the K^+ dissolution curve matched that of the tunnel sites, while the Pb^{2+} dissolution curve corresponded to that of surface adsorption (Figure 3A).[28] This further demonstrates that Pb^{2+} does not enter the tunnel by substituting K^+ during its adsorption on α-MnO_2.

By monitoring the concentrations of aqueous K^+ and Pb^{2+} during Mn^{2+}-induced δ-MnO_2 transformation in the presence of Pb^{2+}, we found that the K^+ concentration continuously increased and substantial K^+ release, which may come from δ-MnO_2 synthesis (Figure 3C). At the initial stage of Pb^{2+} adsorption on δ-MnO_2, approximately 0.6 mM of K^+ was quickly released into the solution. The final K release can reach 0.73 mM after 30 day Pb^{2+} adsorption. In the process of Mn^{2+}-induced δ-MnO_2 aging in the presence of Pb^{2+}, since the initial δ-MnO_2 adsorbed Pb^{2+} (4 h) was washed to remove a large amount of δ-MnO_2 sequestered K^+, only 0.05 mM of K^+ was released in the first few hours and slowly increased to 0.06 mM in the following 30 days. This result indicates that a large amount of K^+ on δ-MnO_2 was largely replaced by Pb^{2+} during the stage of Pb^{2+} adsorption on δ-MnO_2. Subsequently, during the transformation to α-MnO_2, the Pb^{2+} initially adsorbed on δ-MnO_2 becomes further incorporated and stabilized within the tunnels of the newly formed α-MnO_2.

XPS spectroscopy of Mn $2p_{2/3}$ and O 1s was also collected to reveal Mn valence evolution, structural rearrangement, and Mn-phase evolution, and confirm Pb^{2+} migration within the tunnel structure (Figures S8 and S9 and Table S2).[30] Due to the introduction of Mn^{2+}, Mn $2p_{2/3}$ XPS fitting results showed that the average oxidation state of Mn (Mn_{AOS}) decreased from 3.82 to 3.76 (Table S2). Mn(IV) content decreased from 82.32% to 76.56%, while Mn(III) content increased from 17.68% to 23.44% (Table S2). Consistently, titration measurements of the formed products at pH 4 reveal that the bulk Mn_{AOS} initially decreases from ∼3.91 ± 0.02 to ∼3.75 ± 0.02 during the first 7 h. This value rises back to ∼3.90 ± 0.01 at 30 days (Table S3), indicating a transient reduction followed by reoxidation in the materials. This bulk Mn_{AOS} evolution closely mirrors the surface Mn_{AOS} trend observed by XPS, further supporting the δ-to-α-phase transformation of MnO_2. A slight discrepancy in the absolute Mn_{AOS} values obtained by titration vs XPS ones is expected because XPS probes only the surface electronic state while titration reflects the overall bulk redox states. It aligns with a redox reaction where Mn(IV) is reduced to Mn(III) by the introduced Mn^{2+}, leading to the formation of numerous [Mn(III)O_6] units finally contributing to the tunnel walls. It is also consistent with the initial appearance of Pb_α-MnO_2_tun in the XRD patterns (Figure 1B). As the recrystallization progressed, the crystallinity of the Pb_α-MnO_2_tun was improved, with Mn(IV) content increasing to 87.25%, Mn(III) content decreasing to 12.75%, and Mn_{AOS} rising to 3.87, indicating the disproportionation of Mn(III) to Mn(IV) and Mn(II) (Figure S8 and Table S1). The changes in Mn_{AOS} are also consistent with our previous study on the multistage oriented assembly from δ-MnO_2 to α-MnO_2.[16] This suggests that the formation of Pb_α-MnO_2_tun nanorods may follow the same assembly process.

Based on characterization analyses, the schematic illustration of how Pb^{2+} enters the 2 × 2 tunnel structure of α-MnO_2 is proposed (Figure 3D). In step 1, Pb^{2+} adsorbed on the (110) surface of δ-MnO_2 and substantially replaced surface K^+ ions.[31] This displacement leads to a substantial release of K^+ into the solution (Figure 3C). During the Mn^{2+}-induced δ-MnO_2 transformation into α-MnO_2, Pb^{2+} further replaces the trace amounts of K^+ adsorbed on the (110) surface of δ-MnO_2 and participates in the oriented assembly of α-MnO_2 nanorods along the tunnel walls (Figure 1).[16] In step 2, Pb^{2+} serves both as a template cation guiding tunnel wall formation and as a structural stabilizer within the tunnel center (Figure 2). This facilitates the δ-MnO_2 transformation into the coronadite phase, resequestering Pb^{2+} in the 1-D tunnel structure.

https://doi.org/10.1021/acsnano.6c00961
ACS Nano 2026, 20, 11344−11357

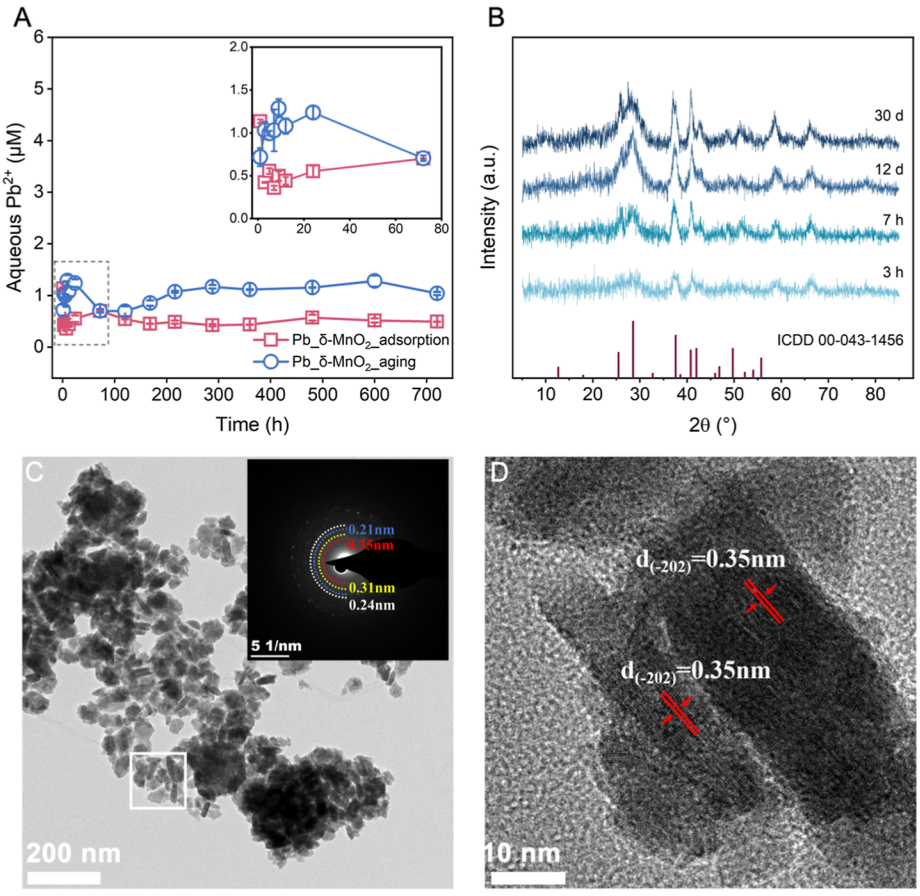

Figure 4. Pb^{2+} adsorption and Mn^{2+}-driven structural evolution of δ-MnO_2 at pH 5.5. (A) Dynamics of aqueous Pb^{2+} concentration change during Pb^{2+} adsorption on δ-MnO_2 and Mn^{2+}-induced δ-MnO_2 aging in the presence of Pb^{2+} at pH 5.5. (B) Time-resolved XRD patterns of solid products collected from Mn^{2+}-induced δ-MnO_2 aging samples in the presence of Pb^{2+} at pH 5.5. Coronadite (ICDD no. 00-043-1456) is plotted as a reference. (C) The HRTEM image of the 30 day reaction solid products from Mn^{2+}-induced δ-MnO_2 aging in the presence of Pb^{2+} at pH 5.5. The SAED image is inserted. (D) The HRTEM zoom image of the selected region displays the lattice fringe of the newly formed α-MnO_2.

Subsequently, due to the H-bonding interactions between hydroxyl groups (−OH) connecting the adjacent [MnO_6] octahedral layers, the [MnO_6] layers come closer and attach to form a tunnel structure, thereby firmly "locking" the Pb^{2+} ions within the 2 × 2 tunnels (Figure 3D). Since each interlayer space between adjacent [MnO_6] octahedral tunnel walls contains a Pb^{2+} ion, the attachment process leads to the release of a small amount of Pb^{2+} ions (Figure 1A). In step 3, the initial Pb_α-MnO_2_tun nanorods further undergo an edge-to-edge oriented assembly process to finally form crystalline α-MnO_2 (Figure S10).

The Effect of pH on the Phase Transformation and the Pb^{2+} Immobilization

Given the proposed structural evolution pathway on Pb^{2+} immobilization within the tunnels of α-MnO_2, it is essential to determine whether this mechanism also operates consistently across different pHs. Accordingly, Pb adsorption onto raw δ-MnO_2 and Mn^{2+}-induced aging of layered δ-MnO_2 in the presence of Pb^{2+} were further investigated over 30 days at pH 5.5 (Figure 4). At pH 5.5, the concentration of aqueous Pb^{2+} during the adsorption and phase transformation process showed a similar trend to that at pH 4 (Figures 1A and 4A). During the initial 1−36 h, the Pb^{2+} concentration increased, followed by a continuous decline (Figure 4A). At the end of the reaction, aqueous Pb^{2+} concentration was approximately 0.45 μM, which was lower than the corresponding value of ∼1.5 μM at pH 4 (Figures 1A and 4A). This suggests that at pH 5.5, Mn^{2+}-induced δ-MnO_2 aging in the presence of Pb^{2+} promotes a structural transformation similar to that observed at pH 4.[32]

XRD patterns indicate that, at pH 5.5, the transformation of δ-MnO_2 to Pb-bearing α-MnO_2 initiates after 3 h of Mn^{2+} addition. With the prolonged reaction time, well-crystallized Pb-bearing α-MnO_2 is eventually formed (Figure 4B). HRTEM image shows the formation of shorter α-MnO_2 nanorods with lengths of merely ∼10−20 nm under pH 5.5 (Figure 4C,D). The corresponding SAED patterns further confirm that these nanorods are well-crystallized α-MnO_2 phase (Figure 4C). These results imply that increasing pH may hinder oriented attachment along the (001) crystal plane, thereby suppressing rapid elongation of the nanorods,[17] which is observed to be ∼100−300 nm in length at pH 4 (Figure 2A).

Our study demonstrated that at pH 5.5, the introduction of Mn^{2+} alone did not induce phase transformation from δ-MnO_2 to α-MnO_2, but instead still maintained it as δ-MnO_2 (Figure S11). The presence of Pb^{2+} induces a clear transformation of δ-MnO_2 to α-MnO_2 at pH 5.5, highlighting the promotive role of Pb^{2+} complexation in the layer-to-tunnel transformation. Structural analyses of the solid products from Pb^{2+} adsorption on δ-MnO_2 without Mn^{2+} addition indicated that Pb^{2+} adsorption alone did not trigger δ-MnO_2 phase transformation

https://doi.org/10.1021/acsnano.6c00961
ACS Nano 2026, 20, 11344−11357

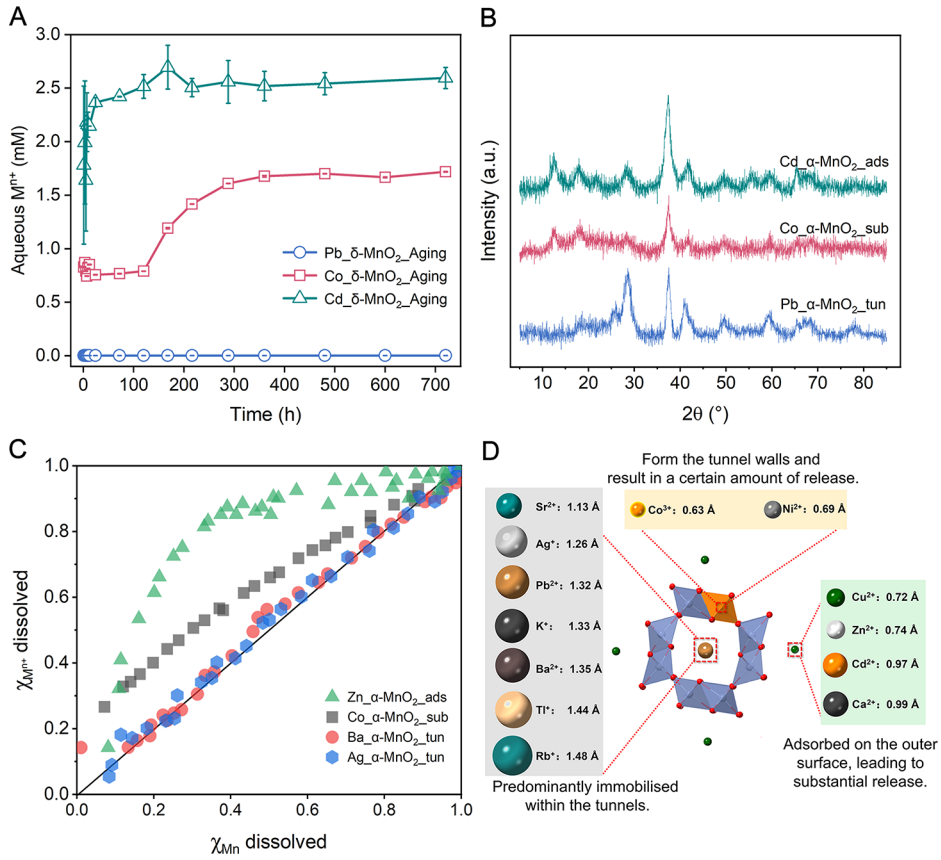

Figure 5. Effect of M^{n+} size on sequestration and release behavior during Mn^{2+}-induced δ-MnO_2 to α-MnO_2 transformation. (A) Dynamics of aqueous M^{n+} concentration change during Mn^{2+}-induced δ-MnO_2 aging in the presence of varied heavy metals (i.e., Pb^{2+}, Cd^{2+}, and Co^{2+}) at pH 4. "M" here represents the metal cations with their valence states denoted as n+. (B) XRD patterns of 30 day Mn^{2+}-induced δ-MnO_2 transformation samples in the presence of Pb^{2+}, Cd^{2+}, or Co^{2+} at pH 4. (C) The dissolution rate curves of M^{n+} (i.e., Zn^{2+}, Co^{2+}, Ba^{2+}, and Ag^{+}) and Mn during the dissolution of Zn_α-MnO_2_ads, Co_α-MnO_2_sub, Ba_α-MnO_2_tun, and Ag_α-MnO_2_tun solid samples using 2 M HCl. (D) A schematic illustration of potential adsorption sites and immobilization/release mechanisms of varied-size heavy metals in the final α-MnO_2 mineral during Mn^{2+}-induced aging and transformation of δ-MnO_2 into α-MnO_2.

into α-MnO_2, but the mineral crystallinity decreased (Figures S7B and S12). A remarkable decrease in diffraction intensities at 37° ($d_{(100)}$ = 0.24 nm) and 65° ($d_{(110)}$ = 0.14 nm) was detected (Figure S7B). This can be attributed to the preferential adsorption of Pb^{2+} at vacancies and edges of the δ-MnO_2 layers, where the formation of new Pb−O and Pb−Mn bonds disrupts the lattice, thus reducing the δ-MnO_2 crystallinity.[33] XPS Mn $2p_{3/2}$ peak fitting analyses demonstrated that the content and variation trend of Mn_{AOS} were highly comparable to those observed at pH 4 (Figure S13 and Table S2). Titration data at pH 5.5 show that the Mn_{AOS} decreases from 3.85 to 3.73 and then rises to 3.91, demonstrating an initial decline followed by a rebound (Table S3). This trend is consistent with the oxidation state changes determined by XPS, further supporting the generation and migration of Mn(III) and the δ-to-α-phase conversion mechanism of MnO_2. In summary, Pb^{2+} adsorption on δ-MnO_2 reduces its crystallinity and destabilizes the Mn−O framework at pH 5.5. At the same time, the Mn(III) generated from the comproportionating reaction between the added Mn^{2+} and structural Mn(IV) is more prone to migrate within the weakened lattice.[17] Finally, Mn(III) can relocate to positions above and below the [MnO_6] octahedral layers, facilitating the tunnel wall construction.[16] This process ultimately promotes the structural transformation and assembly of δ-MnO_2 into α-MnO_2 in the presence of Mn^{2+} and Pb^{2+} together. Pb^{2+} adsorption triggers the Mn^{2+}-induced transformation of stable δ-MnO_2 into α-MnO_2 at pH 5.5, in contrast to the previous observation.[17] In addition, at pH 5.5, the preadsorbed Pb^{2+} on δ-MnO_2 can be strongly sequestered within the tunnels of the α-MnO_2 structure in the presence of Mn^{2+}, like at pH 4.

The Effect of Heavy Metal Atomic Radius on δ-MnO_2 Layer-to-Tunnel Transformation

Given the tunnel structure of α-MnO_2, which has a 2 × 2 framework of edge-sharing [MnO_6] octahedra with a tunnel cross-section of ∼4.6 Å, metal cations with ionic radii smaller than 1.5 Å are suitable for tunnel sequestration (Figure 5D). For example, K^+ (∼1.33 Å) is the native tunnel cation in K-bearing α-MnO_2. Among different heavy metals, large monovalent cations such as Ag^+ and Tl^+ (∼1.26 Å and 1.44 Å, respectively) may easily enter inside the tunnels.[34−37] Large divalent cations such as Sr^{2+} (∼1.13 Å), Ba^{2+} (∼1.35 Å), and Pb^{2+} (1.32 Å) can also match well with the 2 × 2 tunnel structure of α-MnO_2.[33,36−38] Meanwhile, small-sized divalent ions such as Ca^{2+}, Cu^{2+}, Zn^{2+}, Cd^{2+} with radii of ∼0.7−0.95 Å are well below this limit.[14,34,39−41] Due to their relatively small ionic size and strong tendency to be hydrolyzed, these ions might not be effectively accommodated within the tunnels of α-MnO_2. When the ionic size is even smaller, such as Co^{3+} (∼0.63 Å) and Ni^{2+} (∼0.69 Å), they tend to substitute

https://doi.org/10.1021/acsnano.6c00961
ACS Nano 2026, 20, 11344−11357

Mn(IV) (~0.53 Å) in the octahedral lattice. This substitution can enhance the stability of metal ions within the α-MnO_2 structure. However, the number of isomorphic substitutions (or sequestered content) is generally very low.[14,34,39−41]

With these considerations, we tested Cd^{2+} preadsorbed and Co^{2+}-doped δ-MnO_2 as the initial Mn oxides to investigate their fate during the Mn^{2+}-induced transformation experiment at pH 4 or 5.5 (Figure 5). The wet chemistry results indicated substantial release of Cd^{2+} into the solution (about 2.7 mM) after Mn^{2+} was introduced. It demonstrates that Cd^{2+} did not readily enter the tunnel structure of poorly crystalline α-MnO_2 (Figures 5A,B and S14). Furthermore, K^+ remained in the tunnels to form cryptomelane, suggesting that Cd^{2+} did not replace K^+ during the initial adsorption onto δ-MnO_2. The Co^{2+}-doped δ-MnO_2 released approximately 1.7 mM of Co^{2+} upon Mn^{2+} addition and induced transformation, and the Co^{2+}-doping slowed the structural transformation into the highly crystalline α-MnO_2 phase when compared with Pb^{2+} adsorption (Figures 5A−C and S15).

To substantiate the effect of ionic radius, Ba^{2+} (~1.35 Å) and Ag^+ (~1.26 Å), having distinct charges but ionic radii comparable to Pb^{2+} (~1.32 Å), and the small-sized cation Zn^{2+} (~0.74 Å, size-proximal to Cd^{2+} (~0.97 Å)) were preadsorbed onto δ-MnO_2 to further investigate their fate during Mn^{2+}-induced transformation at pH 4. The results demonstrated that the acidic dissolution profiles of Ag^+ and Ba^{2+} were remarkably consistent with that of Pb^{2+} (Figures 3A and 5C), which can only be released after the structural destruction of the newly formed α-MnO_2. Upon complete dissolution, the equilibrium concentrations of Ba^{2+} and Ag^+ reached 0.24 and 0.20 mmol/L, respectively, which are closely aligned with the values observed for Pb^{2+} (Table S1). This indicates that, similar to Pb^{2+}, these metal ions were successfully incorporated into the 2 × 2 tunnels of α-MnO_2 to form hollandite-type structures (Figure S16). In contrast, the dissolution curve of Zn^{2+} exhibited a characteristic convex-upward trend, suggesting its sequestration mainly via surface adsorption on α-MnO_2 (Figure 5C). The final concentration of Zn in the solution was 0.03 mmol/L, matching the adsorption level of Pb^{2+} on α-MnO_2 (Table S1), which confirms that Zn^{2+} failed to enter the structural tunnels and instead remained adsorbed on the cryptomelane surface (Figure S16). Figures 3A and 5C together showed that the incorporation of Pb^{2+}, Ag^+, and Ba^{2+} into the tunnels could be an effective sequestration strategy, and another effective method is the isomorphic substitution of Co^{2+} for Mn within the tunnel walls. In contrast, metal cations like Cd^{2+} and Zn^{2+} that are merely adsorbed on the outer surface of δ-MnO_2 tend to be extensively released during Mn oxide phase transformation, posing a potential risk for secondary heavy metal release (Figure 5D).

Interestingly, our previous study revealed that during the transformation of Na-bearing δ-MnO_2 to α-MnO_2, Na^+ ions (~0.95 Å) could not be stably retained within the tunnels of α-MnO_2.[16] Due to its small ionic radius, the distance between Na^+ and O or Mn atoms in the tunnel is too large to form stable chemical bonds to sequester Na^+, resulting in the formation of unstable empty tunnels. However, at high synthesis temperature, Na^+ can indeed enter the tunnels, leading to the formation of manjiroite.[42] These findings indicate that the ionic radius range of approximately 1.13−1.5 Å might serve as a valid constraint for cation incorporation into tunnel structures of α-MnO_2 at room temperature. Thus, the remediation of different heavy metals by Mn oxides should consider an effective strategy from tunnel sequestration, isomorphic substitution, and surface adsorption based on the metal physicochemical property (Figure 5D).

The sequestration sites and sequestration/release behaviors of varied-sized metal cations during the transformation from δ-MnO_2 to α-MnO_2 are thus proposed and schematically summarized in Figure 5D. Metal cations, which can be effectively immobilized in the α-MnO_2 2 × 2 tunnels, possess typically ionic radii within the range of approximately 1.13−1.5 Å, with suitable coordination structures allowing for the direct substitution for tunnel-bound K^+. Small size or highly charged cations, particularly being prone to hydrolysis, remain excluded or form distinct external phases. The bond strength between the cation and Mn or O of Mn oxides is another critical factor determining its ability to stably reside within the tunnel structure. All factors mentioned above, including cation radius size, chemical properties, and bonding strength, together determine their immobilization potential and stabilization within the tunnel Mn oxide structures.

Taken together, these insights highlight that confining heavy metals within robust tunnel frameworks can serve as a widely applicable strategy for their sequestration and remediation. For example, α-MnO_2 (with 2 × 2 tunnels) is commonly found in acidic environments (pH ~ 2−5.5) and stably sequesters medium-sized metal cations,[17] whereas todorokite (τ-MnO_2, with larger 3 × 3 tunnels) forms under near-neutral to mildly alkaline conditions and can accommodate bulkier hydrated cations such as Cs^+ and La^{3+}.[22,43−45] Similarly, other tunnel-bearing minerals exhibit analogous trapping capabilities: the 2 × 2 tunnels of akaganeite (β-FeOOH) effectively immobilize anions like Cl^-,[46] and the large (>1 nm) channels of clay minerals (e.g., palygorskite and sepiolite) can encapsulate diverse metal cations as well as small organic molecules.[47]

Drawing from these diverse mineral applications and the observed Mn−Pb interactions, crystallization-induced metal fixation appears to be broadly governed by three general principles: (i) dimensional compatibility: where effective sequestration requires a strict geometric match between the pollutant radius and the host lattice cavities; (ii) structural templating: where target cations act as directing agents that stabilize the open framework against collapsing into denser phases; and (iii) topological evolution: where solid-state or oriented attachment pathways favor physical encapsulation, whereas dissolution−reprecipitation pathways may increase the risk of metal release. Ultimately, these mechanistic rules illustrate the generalizability of tunnel confinement for metal pollutant removal and remediation,[48] as demonstrated by the "Synroc" strategy using hollandite-type titanates ($BaAl_2Ti_6O_{16}$) for Cs^+ and Ba^{2+} sequestration,[49,50] the structural stabilization of akaganeite (β-FeOOH) through halide accommodation or isomorphic transition metal substitution (e.g., Ni^{2+}, Co^{2+}),[51] and the selective cation trapping within tungsten bronzes (M_xWO_3).[52] It suggests that this tunnel-based heavy metal immobilization mechanism could be broadly exploited in both natural and engineered systems.

CONCLUSIONS AND IMPLICATIONS

The layer-to-tunnel transformation of δ-MnO_2 to α-MnO_2 provides an unexpected pathway for enhancing heavy metal sequestration and stabilization. These findings challenge the prevailing paradigm that the transition from poorly crystalline minerals with high adsorption to highly crystalline phases with

https://doi.org/10.1021/acsnano.6c00961
ACS Nano 2026, 20, 11344−11357

low adsorption (or from layer-to-tunnel phases) inevitably leads to the release of sequestered heavy metals. By comparing varied size cation behaviors across different complexation sites, including outer surface, tunnel walls, and tunnel interiors, we reveal a new mechanistic understanding of selective metal retention and release strategy via layer-to-tunnel phase transitions. Consequently, this crystallization-induced sequestration is broadly governed by dimensional compatibility, structural templating, and the topological evolution of the phase transformation. These findings not only deepen our current understanding of cation dynamics on Mn oxides but also broaden the implications about metal geochemical cycling, metal remediation strategies, and the design of Mn-based functional materials. This study can serve as a foundation for exploring how crystallographic evolution governs cation geochemical behaviors and highlights future research needs to elucidate further how different tunnel structures, ionic radii, substitution pathways, and environmental matrices collectively dictate long-term cation sequestration stability and strategy.

MATERIALS AND METHODS

Preparation of Initial δ-MnO_2 Samples

7.55 g of $MnSO_4$ was dissolved in 89 mL of Milli-Q water, followed by the addition of 11 mL of acetic acid (CH_3COOH) to obtain a solution with final concentrations of 2 M CH_3COOH and 0.5 M $MnSO_4$, under continuous stirring conditions at room temperature. 6.912 g of $KMnO_4$ was then prepared and dissolved in 100 mL of Milli-Q water to obtain a 0.4375 mol/L $KMnO_4$ solution. The two solutions were mixed thoroughly and immediately filtered. The solid minerals obtained were washed with Milli-Q water using vacuum filtration until the conductivity dropped below 20.0 μS/cm. The synthetic δ-MnO_2 analogue using this preparation method resembles natural Mn oxides in soils. The reaction equation for the δ-MnO_2 synthesis is described as follows. The collected solid materials were further characterized by XRD and identified to be pure δ-MnO_2.[16]

$$2KMnO_4 + 3Mn^{2+} + 2H_2O \rightarrow 2K^+ + 4H^+ + 5MnO_2$$

Pb^{2+} Adsorption on δ-MnO_2 and Mn^{2+}-Induced δ-MnO_2 Transformation to Sequester Pb^{2+}

First, 125 mL of $PbSO_4$ solution was mixed with 125 mL of a δ-MnO_2 suspension to obtain a targeted Mn oxide concentration of 2.4 g/L and a targeted $PbSO_4$ concentration of 3 mmol/L. The $PbSO_4$ solution and Mn oxide suspension were adjusted to pH 4 or 5.5 before mixing. Also, the prepared mixture suspension was frequently adjusted to the targeted pH values (i.e., 4 and 5.5) using 0.01 mol/L H_2SO_4/NaOH during the 30 day adsorption reaction. At the selected time intervals, the solution supernatants and the solid mineral samples were collected via centrifugation and filtration methods, respectively. These adsorption experimental processes are denoted as the metal_δ-MnO_2_ads (Table 1). The same method was applied to perform Pb^{2+} adsorption on α-MnO_2. δ-MnO_2 might usually self-transform into α-MnO_2 at pH < 4 due to its acidic dissolution. In this study, 10 mM Mn^{2+} was added to accelerate the phase transformation of δ-MnO_2. This concentration was selected because 10 mM Mn^{2+} could be representative of high-concentration pollution scenarios, such as acid mine drainage (AMD), where dissolved manganese levels can reach up to 36 mM and mineral transformation and heavy metal sequestration are most critical.[53] Previous research reports that at pH 4, δ-MnO_2 can transform into α-MnO_2 without the addition of Mn^{2+}, but the process occurs at an exceedingly slow rate.[54] 10 mM Mn^{2+} was thus selected here. Additionally, pH 4 and 5.5 are not only suitable for this transformation but also commonly found in environments, such as acidic mine drainage and polluted acidified soils, where manganese oxides and heavy metals co-occur.[17] Thus, pH 4 and 5.5 were selected for our study.

A previous study showed that δ-MnO_2 could transform into α-MnO_2 when the molar ratio of [Mn^{2+}]/[δ-MnO_2] reached 0.36.[17] In this study, Mn^{2+} (i.e., $MnSO_4$ solution) was introduced as an inducer of δ-MnO_2 recrystallization into α-MnO_2. To achieve this induced δ-MnO_2 aging or transformation, the raw δ-MnO_2 preadsorbed Pb^{2+} or other varied heavy metals (i.e., Co^{2+}, Cd^{2+}, Zn^{2+}, Ba^{2+}, and Ag^+) for 4 h was first prepared at a concentration of 2.4 g/L and was then centrifuged at 12,000 rpm and washed twice using Milli-Q water. The obtained wet mineral samples were redispersed in 250 mL of a 10 mmol/L $MnSO_4$ solution to drive the Mn^{2+}-induced δ-MnO_2 crystallization reaction at room temperature. Here, the [Mn^{2+}]/[δ-MnO_2] ratio is around 3.6. During 30 day (Zn^{2+}, Ba^{2+}, and Ag^+ for only 7 day) transformation/aging experiments, the suspension pH was frequently adjusted to the targeted ones (i.e., 4 and 5.5) using 0.01 mol/L H_2SO_4/NaOH. These aging experimental processes are denoted as the metal_δ-MnO_2_Aging (Table 1). After a 30 day reaction or at selected time intervals, the solid mineral samples or the solution supernatants were collected via centrifugation and drying at room temperature, and filtration, respectively. Specifically, for the kinetic experiments of element dynamics (e.g., Pb, Cd, Co, and K), the supernatants were obtained via filtration by passing through a 0.22 μm pore-size membrane filter, and the supernatants were analyzed via the ICP-OES method. The dried solid samples were further characterized via structural and morphological analyses. Experiments of Mn^{2+}-induced δ-MnO_2 aging in the presence of Cd^{2+} and Co^{2+} were performed using the same steps described above (Table 1). The collected solid sample names after 30 day adsorption or transformation are described in the bottom part of Table 1.

Structural Analyses

Powder X-ray Diffraction (XRD). X-ray powder diffraction was used to analyze the crystal structure of Mn oxide minerals and solid products. The synthetic Mn oxides or the reaction intermediate solid products were collected and washed once with Milli-Q water, and the obtained solid minerals were dried at room temperature. X-ray diffraction analysis was then performed using both powder pressing and oriented plate methods. Diffraction analysis was carried out on a Bruker D8 Advance X-ray diffractometer. The test conditions were as follows: Bragg−Brentano diffraction geometry, LynxEye array detector, Ni filter, Cu Kα radiation (λ = 0.15418 nm), tube voltage of 40 kV, tube current of 40 mA, step scan mode with a step size of 0.02°, and a scan rate of 1°/min or 10°/min.

Extended X-ray Absorption Fine Structure (EXAFS). Pb L_3-edge X-ray absorption spectroscopy was collected at the BL14W Beamline at the Shanghai Synchrotron Radiation Facility (SSRF) (Shanghai, China). The data collection was carried out in transmission mode using an ionization chamber for Pb samples, and in transmission mode using a Lytle detector for manganese oxide samples. All spectra were collected under ambient conditions. XAFS data were processed according to the standard procedures using the Athena module implemented in the IFEFFIT software packages. The EXAFS spectra were obtained by subtracting the postedge background from the overall absorption and then normalizing with respect to the edge-jump step. Subsequently, the $\chi(k)$ data were Fourier transformed into real (R) space using a Hanning window (dk = 1.0 $Å^{-1}$) to separate the EXAFS contributions from different coordination shells. To obtain the quantitative structural parameters around central atoms, least-squares curve parameter fitting was performed using the Artemis module of the IFEFFIT software packages. The theoretical scattering paths for Pb L_3-edge fitting were generated using FEFF 6.0 based on hexagonal birnessite (for layered samples) and coronadite-type ($PbMn_3O_8$, space group $P2/c$, Table S4) crystallographic structures. During the optimization in Artemis, we adopted a statistical threshold for ΔE_0 within ±15 eV, a range recognized as acceptable for distorted mineral−metal interfaces. Specifically, for the Pb_α-MnO_2_ads sample, the shell-specific ΔE_0 of −12.4 eV was necessary to compensate for the phase deficit arising from lattice relaxation at the external (310) surfaces. For wavelet transform analysis, the $\chi(k)$ exported from Athena was imported into the Hama Fortran code. The parameters were listed as follows: R-range, 0.0−5.0

https://doi.org/10.1021/acsnano.6c00961
ACS Nano 2026, 20, 11344−11357

Å, k-range, 0−16.0 $Å^{-1}$ for sample and reference standards; k weight, 2; and Morlet function with $\kappa = 8$, $\sigma = 1$ was used as the mother wavelet to provide the overall distribution. Distances in Table 2 are reported as phase-corrected fitted real-space distances (R). When FT peak positions are mentioned, they are explicitly labeled as uncorrected FT peak positions ($R + \Delta R$), which are affected by phase shifts and should not be interpreted as bond lengths.

Morphological Analyses

Field Emission Scanning Electron Microscopy (FESEM). Morphological analysis of varied Mn oxide samples was conducted using a JEOL field emission scanning electron microscope (JSM-6700F). A small amount of powder samples were placed on a conductive adhesive carbon tape, and the sample surface was coated with platinum/gold particles under a vacuum condition. The measurement conditions include the accelerating voltage of 5 kV, the current of 5 μA, and the working distance (WD) of 7.9 mm.

High-Resolution Transmission Electron Microscopy (HRTEM). The HRTEM analysis was performed on a JEM 2100F microscope with an accelerating voltage of 200 kV. A small amount of mineral fine samples was mixed with an appropriate amount of Milli-Q water and sonicated to form a homogeneous suspension. After dispersing, a suitable amount of the suspension was collected using a carbon-coated microgrid, which was then vacuum-dried at room temperature. The grain morphology was captured at lower magnification, and at higher magnification, appropriate diffraction conditions were set to obtain two-dimensional lattice images of the crystals.

Spherical aberration corrected scanning transmission electron microscope (AC-STEM) analysis was performed on a FEI Titan 80-300 environmental high-resolution transmission electron microscope (HRTEM) with an aberration-corrected Titan Krios 300 kV equipped with a 300 keV cold-field emission gun and a high-angle annular dark-field imaging (HAADF) detector. Energy dispersive X-ray spectroscopy (EDS) was performed by FEI Talos F200S X-ray detector and FEI X-CFEG Spectra Ultra X-ray detector. The images are processed using fast Fourier transform (FFT) and inverse fast Fourier transform (IFFT) methods as required to determine the atomic arrangement symmetry and identify defects within the crystal lattice.

Wet Chemistry Analysis

Inductively Coupled Plasma Optical Emission Spectrometer (ICP-OES). Elemental content (i.e., Pb, Cd, Co, Ag, Ba, Zn, K, and Mn) of the supernatants or acid-dissolved samples during the reaction was determined using an Agilent 5800 instrument.

■ ASSOCIATED CONTENT

Supporting Information

The Supporting Information is available free of charge at https://pubs.acs.org/doi/10.1021/acsnano.6c00961.

Texts S1−S5: experiments of DFT and XPS methods, Pb adsorption and acid dissolution, Mn_{AOS} titration; Figures S1−S16: dissolved Mn^{2+} and metal adsorption, HRTEM−EDS images, Pb L_3-edge EXAFS spectroscopy and its wavelet transform, XRD patterns, XPS spectroscopy; SEM images; a schematic illustration of metal sequestration; Tables S1−S4: acidic dissolution composition, XPS fitting results, titration Mn_{AOS}, and coronadite-type ($PbMnO_3$, space group $P2/c$) crystallographic structures (PDF)

■ AUTHOR INFORMATION

Corresponding Authors

Xinran Liang − *College of Resources and Environment, Yunnan Agricultural University, Kunming, Yunnan 650000, China; The Key Laboratory of Soil Health and Green Remediation, Ministry of Ecology and Environment, College of Resources and Environment, Huazhong Agricultural University, Wuhan 430070, China*; Email: 2020015@ynau.edu.cn

Xionghan Feng − *The Key Laboratory of Soil Health and Green Remediation, Ministry of Ecology and Environment, College of Resources and Environment, Huazhong Agricultural University, Wuhan 430070, China*; orcid.org/0000-0001-5499-7174; Email: fxh73@mail.hzau.edu.cn

Biao Wan − *The Key Laboratory of Soil Health and Green Remediation, Ministry of Ecology and Environment, College of Resources and Environment, Huazhong Agricultural University, Wuhan 430070, China*; orcid.org/0000-0003-2903-1655; Email: biao.wan@mail.hzau.edu.cn

Authors

Xinyu Gao − *College of Resources and Environment, Yunnan Agricultural University, Kunming, Yunnan 650000, China*

Haoran Hu − *College of Resources and Environment, Yunnan Agricultural University, Kunming, Yunnan 650000, China*

Muammar Mansor − *Geomicrobiology, Department of Geosciences, University of Tübingen, Tübingen 72076, Germany*

Fayang Guo − *Institute of Resources & Environment, Henan Polytechnic University, Jiaozuo 454000, China*; orcid.org/0000-0001-7146-3756

Bruno Lanson − *CNRS ISTerre, University of Grenoble Alpes, Grenoble F-38000, France*; orcid.org/0000-0003-1187-3221

Lei Wang − *College of Resources and Environment, Yunnan Agricultural University, Kunming, Yunnan 650000, China*; orcid.org/0000-0003-1766-7429

Fangdong Zhan − *College of Resources and Environment, Yunnan Agricultural University, Kunming, Yunnan 650000, China*

Yanqun Zu − *College of Resources and Environment, Yunnan Agricultural University, Kunming, Yunnan 650000, China*

Haesung Jung − *Department of Battery and Chemical Engineering, Changwon National University, Changwon, Gyeongsangnam-do 51140, Republic of Korea*

Hui Li − *Department of Crop and Soil Sciences, North Carolina State University, Raleigh, North Carolina 27695, United States*; orcid.org/0000-0002-9374-5305

Wenfeng Tan − *The Key Laboratory of Soil Health and Green Remediation, Ministry of Ecology and Environment, College of Resources and Environment, Huazhong Agricultural University, Wuhan 430070, China*

James J. De Yoreo − *Physical Sciences Division, Pacific Northwest National Laboratory, Richland, Washington 99352, United States*; orcid.org/0000-0002-9541-733X

Complete contact information is available at: https://pubs.acs.org/10.1021/acsnano.6c00961

Notes

The authors declare no competing financial interest.

■ ACKNOWLEDGMENTS

This work was supported by grants from the National Natural Science Foundation of China (42367005, 42407326, 42377303, and W2521004). B.W. acknowledges financial support from Distinguished Young Scholars of the National

Natural Science Foundation of China (Overseas) and the Fundamental Research Funds for the Central Universities-Huazhong Agricultural University. We thank Prof. James De Yoreo for his time and support at PNNL.

REFERENCES

(1) Liu, Z.-T.; Ma, R.; Zhu, D.; Konstantinidis, K. T.; Zhu, Y.; Zhang, S. Organic Fertilization Co-selects Genetically Linked Antibiotic and Metal(loid) Resistance Genes in Global Soil Microbiome. *Nat. Commun.* **2024**, *15*, 5168.
(2) Lefkowitz, J. P.; Rouff, A. A.; Elzinga, E. J. Influence of pH on the Reductive Transformation of Birnessite by Aqueous Mn(II). *Environ. Sci. Technol.* **2013**, *47*, 10364−10371.
(3) Zhao, H.; Zhu, M.; Li, W.; Elzinga, E. J.; Villalobos, M.; Liu, F.; Zhang, J.; Feng, X.; Sparks, D. L. Redox Reactions Between Mn(II) and Hexagonal Birnessite Change its Layer Symmetry. *Environ. Sci. Technol.* **2016**, *50*, 1750−1758.
(4) Yang, R.; Fan, Y. Y.; Ye, R. Q.; Tang, Y. X.; Cao, X. H.; Yin, Z. Y.; Zeng, Z. Y. MnO_2-based Materials for Environmental Applications. *Adv. Mater.* **2021**, *33*, 2004862.
(5) Liang, X.; Zhao, Z.; Zhu, M.; Liu, F.; Wang, L.; Yin, H.; Qiu, G.; Cao, F.; Liu, X.; Feng, X. Self-assembly of Birnessite Nanoflowers by Staged Three-Dimensional Oriented Attachment. *Environ. Sci.:Nano* **2017**, *4*, 1656−1669.
(6) Wang, X.; Peng, J.; Liang, X.; Zhu, M.; Lanson, B.; Wang, L.; Liang, X.; Liu, F.; Tan, W.; Feng, X. Effects of Mn^{2+}, Ni^{2+}, and Cu^{2+} on the Formation and Transformation of Hydrosulfate Green Rust: Reaction Processes and Underlying Mechanisms. *ACS Earth Space Chem.* **2019**, *3*, 519−530.
(7) Wan, B.; Liang, X.; Hu, Z.; Yan, Y.; Tan, W.; Feng, X. Effects of Particle Size and Mineral Crystallinity on Formation of Zn-Al Layered Double Hydroxides (LDH) on Aluminum (oxyhydr) Oxides. *Appl. Clay Sci.* **2021**, *201*, 105933.
(8) Karimian, N.; Hockmann, K.; Planer-Friedrich, B.; Johnston, S. G.; Burton, E. D. Antimonate Controls Manganese(II)-Induced Transformation of Birnessite at a Circumneutral pH. *Environ. Sci. Technol.* **2021**, *55*, 9854−9863.
(9) Wang, Q.; Yang, P.; Zhu, M. Effects of Metal Cations on Coupled Birnessite Structural Transformation and Natural Organic Matter Adsorption and Oxidation. *Geochem. Cosmochim. Acta* **2019**, *250*, 292−310.
(10) Zheng, J.; Xie, Y.; Ping, Y.; Xu, H.; Li, Q.; Liao, Q.; Li, Q.; Yang, Z.; Yang, W.; Si, M. Crystal Phase Conversion of Amorphous Fe-Mn Binary Oxides Promote the Sequestration and Redistribution of Arsenic, Cadmium, and Lead in the Soil: Comparison with Crystalline Form. *J. Environ. Chem. Eng.* **2024**, *12*, 113342.
(11) Hu, M.; Sun, H.; Luo, J.; Chen, S.; Li, D. The Superior Adsorption Capacity of Biogenic α-Mn_2O_3 in Comparison to Chemogenic α-Mn_2O_3 for Five Divalent Heavy Metal Cations and the Adsorption Mechanism of Biogenic α-Mn_2O_3: Experimental and DFT Investigations. *J. Environ. Chem. Eng.* **2024**, *12*, 114029.
(12) Shi, M.; Min, X.; Ke, Y.; Lin, Z.; Yang, Z.; Wang, S.; Peng, N.; Yan, X.; Luo, S.; Wu, J.; Wei, Y. Recent Progress in Understanding the Mechanism of Heavy Metals Retention by Iron (oxyhydr) Oxides. *Sci. Total Environ.* **2021**, *752*, 141930.
(13) Heo, J.; Jung, H. Tailoring Oxidation State of Manganese Enables the Direct Formation of Todorokite. *ACS Nano* **2025**, *19* (13), 12910−12919.
(14) Wu, Z.; Peacock, C. L.; Lanson, B.; Yin, H.; Zheng, L.; Chen, Z.; Tan, W.; Qiu, G.; Liu, F.; Feng, X. Transformation of Co-containing Birnessite to Todorokite: Effect of Co on the Transformation and Implications for Co Mobility. *Geochem. Cosmochim. Acta* **2019**, *246*, 21−40.
(15) Zhao, W.; Tan, W.; Wang, M.; Xiong, J.; Liu, F.; Weng, L.; Koopal, L. K. CD-MUSIC-EDL Modeling of Pb^{2+} Adsorption on Birnessites: Role of Vacant and Edge Sites. *Environ. Sci. Technol.* **2018**, *52*, 10522−10531.
(16) Liang, X.; Post, J. F.; Lanson, B.; Wang, X.; Zhu, M.; Liu, F.; Tan, W.; Feng, X.; Zhu, G.; Zhang, X.; De Yoreo, J. J. Coupled Morphological and Structural Evolution of δ-MnO_2 to α-MnO_2 Through Multistage Oriented Assembly Processes: The Role of Mn(III). *Environ. Sci.:Nano* **2020**, *7*, 238.
(17) Bi, L.; Hu, H.; Wang, L.; Li, Z.; Zhan, F.; He, Y.; Zu, Y.; Li, Y.; Liang, X. Effect of Mn^{2+} Concentration on the Growth of δ-MnO_2 Crystals under Acidic Conditions. *Geochem. Trans.* **2024**, *25*, 9.
(18) Lefkowitz, J. P.; Rouff, A. A.; Elzinga, E. J. Influence of pH on the Reductive Transformation of Birnessite by Aqueous Mn(II). *Environ. Sci. Technol.* **2013**, *47*, 10364−10371.
(19) Feng, X. H.; Zhai, L.; Tan, W.; Liu, F.; He, J. Adsorption and Redox Reactions of Heavy Metals on Synthesized Mn Oxide Minerals. *Environ. Pollut.* **2007**, *147*, 366−373.
(20) Zhao, W.; Wang, Q.; Liu, F.; Qiu, G.; Tan, W.; Feng, X. Pb^{2+} Adsorption on Birnessite Affected by Zn^{2+} and Mn^{2+} Pretreatments. *J. Soils Sediments* **2010**, *10*, 870−878.
(21) Jung, H.; Taillefert, M.; Sun, J.; Wang, Q.; Borkiewicz, O. J.; Liu, P.; Yang, L.; Chen, S.; Chen, H.; Tang, Y. Redox Cycling Driven Transformation of Layered Manganese Oxides to Tunnel Structures. *J. Am. Chem. Soc.* **2020**, *142*, 2506−2513.
(22) Sasaki, K. Synthesis of a Biotemplated Lithium Ion-Sieve Derived from Fungally Formed Birnessite. In *Advances in the Environmental Biogeochemistry of Manganese Oxides*; Feng, X. H., Li, W., Zhu, M. Q., Sparks, D. L., Eds.; American Chemical Society: WA, 2015; Vol. *1197*, pp 169−183.
(23) Manceau, A.; Marcus, M. A.; Grangeon, S. Determination of Mn Valence States in Mixed-Valent Manganates by XANES Spectroscopy. *Am. Mineral.* **2012**, *97*, 816−827.
(24) Zhou, X.; Min, Y.; Zhao, C.; Chen, C.; Ke, M.; Xu, S.; Chen, J.; Wu, Y.; Yu, H. Constructing Sulfur and Oxygen Super Coordinated Main-Group Electrocatalysts for Selective and Cumulative H_2O_2 Production. *Nat. Commun.* **2024**, *15*, 193.
(25) Krivanek, O. L.; Chisholm, M. F.; Nicolosi, V.; Pennycook, T. J.; Corbin, G. J.; Dellby, N.; Murfitt, M. F.; Own, C. S.; Szilagyi, Z. S.; Oxley, M. P.; Pantelides, S. T.; Pennycook, S. J. Atom-by-atom Structural and Chemical Analysis by Annular Dark-field Electron Microscopy. *Nature* **2010**, *464*, 571−574.
(26) Yuan, Y.; Wood, S. M.; He, K.; Yao, W.; Tompsett, D.; Lu, J.; Nie, A.; Islam, M. S.; Shahbazian-Yassar, R. Atomistic Insights into the Oriented Attachment of Tunnel-Based Oxide Nanostructures. *ACS Nano* **2016**, *10*, 539−548.
(27) Yuan, Y.; Liu, C.; Byles, B. W.; Yao, W.; Song, B.; Cheng, M.; Huang, Z.; Amine, K.; Pomerantseva, E.; Shahbazian-Yassar, R.; Lu, J. Ordering Heterogeneity of $[MnO_6]$ Octahedra in Tunnel-Structured MnO_2 and Its Influence on Ion Storage. *Joule* **2019**, *3*, 471−484.
(28) Yin, H.; Li, H.; Wang, Y.; Ginder-Vogel, M.; Qiu, G.; Feng, X.; Zheng, L.; Liu, F. Effects of Co and Ni Co-doping on the Structure and Reactivity of Hexagonal Birnessite. *Chem. Geol.* **2014**, *381*, 10−20.
(29) Wang, F.; Zheng, Y.; Zhu, H.; Wu, T. Screening of MnO_2 with Desired Facet and its Behavior in Highly Selective Adsorption of Aqueous Pb (II): Theoretical and Experimental Studies. *Chemosphere* **2023**, *337*, 139239.
(30) Atkins, B.; Kalu, S.; Li, H. Characterizing the Effect of pH and Molecular Structure on the Reactions of Catechol and Hydroquinone with Birnessite. *Environ. Sci. Technol.* **2025**, *59*, 27279−27290.
(31) Manceau, A.; Steinmann, S. M. Nature of High- and Low-Affinity Metal Surface Sites on Birnessite Nanosheets. *ACS Earth Space Chem.* **2021**, *5*, 66−79.
(32) Zhu, X.; Xu, J.; Zhang, Q.; Shen, T.; Zhuang, Y.; Chen, T.; Li, S.; Gu, L.; Xia, H. Regulating Na Content and Mn Defects in Birnessite for High-Voltage Aqueous Sodium-ion Batteries. *Nat. Commun.* **2025**, *16*, 3838.
(33) Karimian, N.; Hockmann, K.; Planer-Friedrich, B.; Johnston, S. G.; Burton, E. D. Antimonate Controls Manganese(II)-Induced Transformation of Birnessite at a Circumneutral pH. *Environ. Sci. Technol.* **2021**, *55*, 9854−9863.

https://doi.org/10.1021/acsnano.6c00961
ACS Nano 2026, 20, 11344−11357

(34) Nightingale, E. R., Jr. Phenomenological Theory of Ion Solvation. Effective Radii of Hydrated Ions. *J. Phys. Chem.* **1959**, *63*, 1381−1387.
(35) Chen, W.; Liu, J.; Huangfu, X.; Chen, Y.; Zhong, W.; Liu, Y.; Huang, Y.; Liu, H. Reductive Transformation of MnO_2 Controls Thallium Remobilization: Differential Effects of Layered and Tunneled Structures. *Environ. Sci. Technol.* **2025**, *59*, 9221−9234.
(36) Li, C.; Yuan, Y.; Li, P.; Yang, K.; Ren, Q.; Nie, A.; Liu, S.; Lazar, S.; Meingast, A.; Wang, S. Atomic Mechanisms of Cation Adsorption/Exchange in Octahedral Molecular Sieves. *ACS Nano* **2022**, *16* (12), 21618−21625.
(37) Housel, L. M.; Wang, L.; Abraham, A.; Huang, J.; Renderos, G. D.; Quilty, C. D.; Brady, A. B.; Marschilok, A. C.; Takeuchi, K. J.; Takeuchi, E. S. Investigation of α-MnO_2 Tunneled Structures as Model Cation Hosts for Energy Storage. *Acc. Chem. Res.* **2018**, *51*, 575−582.
(38) Mammeri, S.; Halimi, O.; Sebais, M.; Touahri, S.; Boundine, B.; Azizi, A.; Soltani, T. M. The Effect of Sr-Doping on Structural, Optical, Catalytic, and Photocatalytic Properties of α-MnO2 Nanowires Synthesized via a Hydrothermal Route. *Phys. Chem. Res.* **2023**, *11*, 559−574.
(39) Wu, Z.; Lanson, B.; Feng, X.; Yin, H.; Qin, Z.; Wang, X.; Tan, W.; Chen, Z.; Wen, W.; Liu, F. Transformation of Ni-containing Birnessite to Tectomanganate: Influence and Fate of Weakly Bound Ni(II) Species. *Geochem. Cosmochim. Acta* **2020**, *271*, 96−115.
(40) Truong, T. T.; Liu, Y.; Ren, Y.; Trahey, L.; Sun, Y. Morphological and Crystalline Evolution of Nanostructured MnO_2 and Its Application in Lithium-Air Batteries. *ACS Nano* **2012**, *6* (9), 8067−8077.
(41) Davis, D. J.; Lambert, T. N.; Vigil, J. A.; Rodriguez, M. A.; Brumbach, M. T.; Coker, E. N.; Limmer, S. J. Role of Cu-Ion Doping in Cu-α-MnO_2 Nanowire Electrocatalysts for the Oxygen Reduction Reaction. *J. Phys. Chem. C* **2014**, *118*, 17342−17350.
(42) Chang, C.; Yan, Z.; Zhang, C.; Zhang, Y.; Jiang, M.; Ruan, L.; Xiao, M.; Yu, Y.; He, H. Design of Ca-type Todorokite Catalysts with Highly Active for the Selective Reduction of NOx by NH3 at Low Temperatures. *J. Environ. Sci.* **2024**, *138*, 697−708.
(43) Cui, H.; Feng, X.; He, J.; Tan, W.; Liu, F. Effects of Reaction Conditions on the Formation of Todorokite at Atmospheric Pressure. *Clays Clay Miner.* **2006**, *54*, 605−615.
(44) Min, S.; Kim, Y. Adsorption Characteristics of Cs and Cation Selectivity of Todorokite. *Colloids Surf., A* **2022**, *650*, 129652.
(45) Kim, J.; Kwon, K. D. Tunnel Cation and Water Structures of Todorokite: Insights into Metal Partitioning and Isotopic Fractionation. *Geochem. Cosmochim. Acta* **2022**, *333*, 153−165.
(46) Liu, L.; Sassi, M.; Zhang, X.; Nakouzi, E.; Kovarik, L.; Xue, S.; Jin, B.; Rosso, K. M.; De Yoreo, J. J. Understanding the Mechanisms of Anisotropic Dissolution in Metal Oxides by Applying Radiolysis Simulations to Liquid-phase TEM. *Proc. Natl. Acad. Sci. U.S.A.* **2023**, *120* (23), No. e2101243120.
(47) Ruiz, A. I.; Ruiz-García, C.; Ruiz-Hitzky, E. From Old to New Inorganic Materials for Advanced Applications: The Paradigmatic Example of the Sepiolite Clay Mineral. *Appl. Clay Sci.* **2023**, *235*, 106874.
(48) Yang, P.; Post, J. F.; Wang, Q.; Xu, W.; Geiss, R.; McCurdy, P. R.; Zhu, M. Metal Adsorption Controls Stability of Layered Manganese Oxides. *Environ. Sci. Technol.* **2019**, *53*, 7453−7462.
(49) Ringwood, A. E.; Kesson, S. E.; Ware, N. G.; Hibberson, W.; Major, A. Immobilisation of High-Level Nuclear Reactor Wastes in SYNROC. *Nature* **1979**, *278*, 219−223.
(50) Carter, M. L.; Vance, E. R.; Chinoweth, H. R.; Day, R. A.; Loi, E.; Weirich, A. Hollandite-Rich Ceramic Melts for the Immobilisation of Cs and Ba. *J. Nucl. Mater.* **2004**, *327*, 127−136.
(51) Ford, R. G.; Bertsch, P. M.; Farley, K. J. Changes in Transition and Heavy Metal Partitioning during Hydrous Iron Oxide Aging. *Environ. Sci. Technol.* **1997**, *31*, 2028−2033.
(52) Whittingham, M. S.; Guo, J.; Chen, R.; Chirayil, T.; Janauer, G.; Zavalij, P. The Hydrothermal Synthesis of Tungsten Oxide Bronzes. *Solid State Ionics* **1995**, *75*, 257−268.
(53) Ouaddari, H.; Karim, A.; Achiou, B.; Saja, S.; Aaddane, A.; Bennazha, J.; El Amrani El Hassani, I.; Ouammou, M.; Albizane, A. New low-cost ultrafiltration membrane made from purified natural clays for direct Red 80 dye removal. *J. Environ. Chem. Eng.* **2019**, *7*, 103268.
(54) Grangeon, S.; Lanson, B.; Lanson, M. Solid-state Transformation of Nanocrystalline Phyllomanganate into Tectomanganate: Influence of Initial Layer and Interlayer Structure. *Acta Crystallogr., Sect. B: Struct. Sci., Cryst. Eng. Mater.* **2014**, *70*, 828−838.

https://doi.org/10.1021/acsnano.6c00961
ACS Nano 2026, 20, 11344−11357